energies

MDPI

Article

Monitoring of Thermal and Flow Processes in the Two-Phase Spray-Ejector Condenser for Thermal Power Plant Applications

Paweł Madejski [1], Piotr Michalak [1,*], Michał Karch [1], Tomasz Kuś [1] and Krzysztof Banasiak [2]

[1] Department of Power Systems and Environmental Protection Facilities, Faculty of Mechanical Engineering and Robotics, AGH University of Science and Technology, Al. Mickiewicza 30, 30-059 Kraków, Poland
[2] SINTEF Energy, 7034 Trondheim, Norway
* Correspondence: pmichal@agh.edu.pl

Abstract: The paper deals with the problem of accurate measuring techniques and experimental research methods for performance evaluation of direct contact jet-type flow condensers. The nominal conditions and range of temperature, pressure and flow rate in all characteristic points of novel test rig installation were calculated using the developed model. Next, the devices for measurement of temperature, pressure and flow rate in a novel test rig designed for testing the two-phase flow spray ejector condensers system (SEC) were studied. The SEC can find application in gas power cycles as the device dedicated to condensing steam in exhaust gases without decreasing or even increasing exhaust gas pressure. The paper presents the design assumptions of the test rig, its layout and results of simulations of characteristic points using developed test rig models. Based on the initial thermal and flow conditions, the main assumptions for thermal and flow process monitoring were formulated. Then, the discussion on commercially available measurement solutions was presented. The basic technical parameters of available sensors and devices were given, discussed with details.

Keywords: direct contact condenser; spray-ejector condenser; mass flow measurement; experimental test rig

Citation: Madejski, P.; Michalak, P.; Karch, M.; Kuś, T.; Banasiak, K. Monitoring of Thermal and Flow Processes in the Two-Phase Spray-Ejector Condenser for Thermal Power Plant Applications. *Energies* **2022**, *15*, 7151. https://doi.org/10.3390/en15197151

Academic Editor: Ron Zevenhoven

Received: 29 July 2022
Accepted: 26 September 2022
Published: 28 September 2022

1. Introduction

Due to the growing importance of heat and electricity generation efficiency in thermal power plants, while taking into account recent political determinants and resulting legal regulations, especially on CO_2 emissions, various solutions have been developed in recent years.

Ziembicki et al. [1] analysed heat recovery from combustion gases in heating plants using gaseous and liquid fuels. Tic and Guziałowska-Tic [2] investigated the cost-efficiency dependence of the combustion of solid fuel improvement in power boilers, especially fine coal.

Apart from these efficiency-related measures, techniques are also used aiming at a reduction in CO_2 emissions [3,4]. From them, an important role plays carbon capture and storage (CCS) utilising pre-combustion, post-combustion or oxyfuel combustion approaches [5,6].

A pure CO_2 stream from the combustion gases, when combusting the carbonaceous fuel in thermal power plants, can be achieved involving post-combustion and oxy-combustion processes [7].

In [8], authors presented the performance analysis of a designed advanced ultra-supercritical (A-USC) coal-fired 700 MW power plant. To reduce CO_2 emissions, the post-combustion carbon capture and storage (CCS) unit, with a CO_2 removal rate of 90%, was considered. The calculated net efficiency of an A-USC unit was 47.6% and 36.8% with and without CCS, respectively. The electricity output penalty was 362.3 kWh_{el}/tCO_2. However, application of the oxy-combustion method may result in a lower penalty, around 4% [9].

An interesting concept is a power plant based on biomass, which has zero net emission and is connected with CCS and results in negative emissions [7]. Further development of

this idea for sewage sludge in combination with oxy-combustion and CO_2 capture was presented in [10–12]. The whole system consists of three basic parts. In the first of them, sewage sludge is processed into syngas. Next, the resulting fuel is burned in pure oxygen in a special wet combustion chamber. Finally, produced hot steam and carbon dioxide are supplied to a gas turbine cooperating with a spray ejector condenser (SEC) with CO_2 capture. The main task of SEC is to condense the water vapour from the exhaust gases while creating a compact system structure.

Spray condensers (spray ejector condensers, direct contact condensers, jet condensers) have been used in industry since the beginning of the 20th century [13], covering a wide range of various applications in chemical engineering, water desalination, air conditioning and energy conversion processes.

Regarding the latter, in power plants, SECs were used to improve performance and to obtain lower operating costs, and numerous studies on these issues were presented recently.

Desideri and Di Maria [14] simulated the impact of the geothermal fluid main characteristics on the performance of 20 and 60 MW geothermal power plants. Direct contact condensers were used to condense and separate geothermal steam from the non-condensable gases. In [15], waste heat from a thermoelectric power plant was utilised to produce fresh water in a diffusion driven desalination facility using a direct contact condenser. The saturated air and vapour mixture is cooled and dehumidified by the water inside the condenser. Another application of SEC was a cooling cycle in a combined cooling, heat and power (CCHP) system based on a micro-steam turbine and devoted to a residential building [16]. Marugán-Cruz et al. [17] modelled a cooling system involving a direct contact jet condenser to reduce the water consumption of a concentrated solar tower power plant. In [18], authors analysed steam consumption of conventional lignite pre-drying systems when using heat recovery from the process of wet flue gas desulphurisation (WFGD). The WFGD tower was used as a direct-contact heat exchanger and the source of heat for the first pre-drying stage. Zhao et al. [19] simulated heat recovery from flue gas in a gas fired CHP plant with a steam driven absorption heat pump and a direct contact heat exchange tower. In [20], authors applied the O_2/CO_2 cycle to a natural gas combined cycle (NGCC) using a gas turbine. The required oxygen was produced by an air separation unit including a spray condenser. Simulations in Aspen Plus resulted in a net efficiency loss of 8.1%-points when applying separation of CO_2.Garlapalli et al. [21] analysed CO_2 capture from a coal-fired power plant. To reduce the reboiler energy consumption, they proposed a new solution for heat recovery from the flue gas, using a direct contact heat exchanger. The latter was also involved in post-combustion CO_2 capture.

Contrary to numerous simulation works covering a wide range of direct contact condensers, only a limited number of case studies were based on in situ measurements. Wei et. al. [22] analysed a flue gas heat recovery system in a coal-fired CHP. They applied heat recovery with direct-contact cooling with low-temperature water from the heat pump. This heat was used then in a heating network. In [23], authors investigated the utilisation of available excess steam in a 200 MW geothermal power plant with a dry steam cycle. The spray ejector condenser was used to condense the water vapour from the exhaust gases. The simulation model was then validated against operational data and optimisation of the power plant was carried out.

There is a lack of laboratory scale test rigs devoted to measurements for a spray condenser for application in CO_2 capture. Papers were presented on various applications of direct contact condensers in thermal engineering, as pyrolysis of biomass [24], refrigeration cycle [25,26] or directed into construction details, performance characteristics or transient behaviour of SEC [27–30].Therefore, there is a need to experimentally investigate an application of a spray condenser in a CO_2 capture system in a thermal power plant cycle. From a practical point of view, the choice of measurement methods and instruments is important. This issue was also poorly represented in the publications presented. Authors mainly focused on the description of the equipment used together with values of measurement errors. This is the research gap that defines the aim of the paper.

The next section briefly presents the main assumptions for the conceptual design of a test rig developed within the scope of the project for a negative CO_2 emission gas power plant [31–33]. The circuit layout and preliminary simulations are also described. Then, the variability ranges of thermal and flow parameters in the selected points of the test rig are given. This way, the basis to determine appropriate thermal and flow measurement devices is defined. To properly choose the right solution, a short review of the available techniques and methods is also presented. Based on the given background, the design of the proposed test rig is presented, and final conclusions are given.

2. Materials and Methods

2.1. Conceptual Design of the Test Rig

The considered test rig is a part of the developed cycle of a negative CO_2 emission power plant using gasified sewage sludge as a main fuel—the assumptions and scheme of which were presented recently [11,12].

As the main theoretical assumptions of the whole system are known, the main aim of the part presented here was to develop a prototype research installation to study the performance of a spray-ejector condenser. Madejski et al. presented [32,33]; the study includes a description of the concept, schematics, operating ranges, proposals for acquisition and monitoring of operating parameters and basic assumptions for the implementation of the spray-ejector condenser installation. This applies in particular to the condensation of water vapour contained in a gas mixture (e.g., CO_2) and to the generation of a pressure rise in the gas mixture.

Based on the analysis of the sources presented in the introductory part, in order to build the test stand enabling the planned scope of research independently on other components, it was proposed to build a system with the necessary additional subsystems:

- Superheated steam generation system (I).
- CO_2 supply and mixing system (II).
- Spray ejector condenser with the water supplying system (III).
- Tank for water/steam/CO_2 mixture separation into gaseous and liquid parts with their common inlet and separate outlets (IV).
- Connection system between the spray ejector condenser and other parts (V).
- Measurement and monitoring system with data acquisition (VI).

A schematic diagram of the proposed test stand with all additional subsystems, in the form of a simulation model in Ebsilon software, is given in Figure 1. This model was then used to establish the minimum and maximum values of thermal and flow variables in the circuit necessary for the design of the test rig and the selection of the necessary measurement equipment. For the proposed nominal operating conditions of SEC, the thermal capacity of the proposed direct contact type condenser was around 22.5 kW and represents mainly the thermal energy of condensed steam.

The conceptual design of the prototype test stand included assumptions necessary to perform tests on a spray ejector condenser, especially the possibility of supplying the condenser with a liquefied medium (water vapour/CO_2 mixture) and with cooling water, discharging the mixture in the form of water/water vapour/CO_2 and separation of the gaseous part from the liquid (water) part. All tests will be supported by controlling and monitoring selected plant parameters.

The first subsystem is responsible for generating and supplying superheated steam with the possibility of temperature, pressure and steam mass flow control. It consists of a tank with distilled water (or a water treatment plant), a superheated steam generator with capacity regulation, an electric heater for additional steam superheating and necessary sensors of steam pressure, temperature and mass flow.

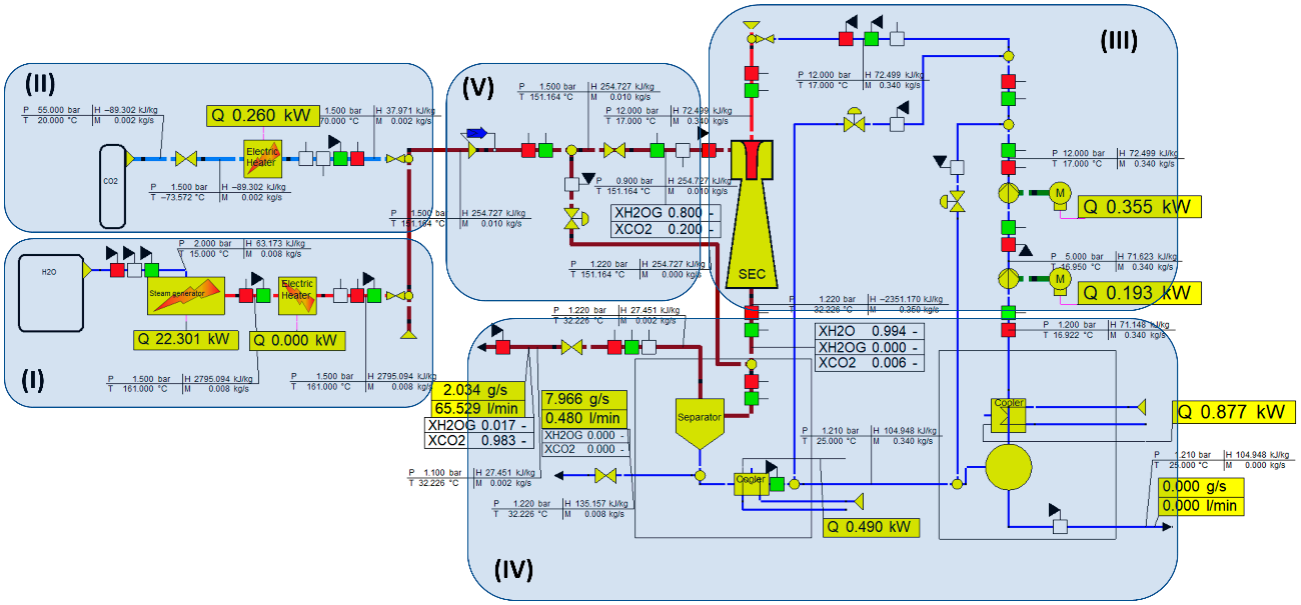

Figure 1. The concept of the designed test stand with the spray ejector condenser performances analysis opportunities. Superheated steam generation system (**I**), CO_2 supply and mixing system (**II**), spray-ejector condenser with the water supplying system (**III**), tank for water/steam/CO_2 mixture separation into gaseous and liquid parts with their common inlet and separate outlets (**IV**), connection system between the spray-ejector condenser and other parts (**V**).

The main task of the second subsystem is to deliver CO_2 with adjustable temperature, pressure and mass flow, together with the CO_2-steam mixing. It is built from a set of liquid CO_2 cylinders with the necessary equipment, an electric heater to warm up CO_2 after its expansion in order to prevent freezing, pressure, temperature and CO_2 mass flow sensors and mixing valves enabling the injection of CO_2 into the steam.

The third system is designed to supply the spray condenser with water at adjustable temperature, pressure and mass flow. It consists of a tank with water supplying a condenser and a cooler to decrease the water temperature, a supplying pump with controlled capacity, two bypasses to adjust water flow rate, and pressure, temperature and water flow rate sensors.

The next part enables separation of the water/steam/CO_2 mixture into gas and liquid parts along with the discharge of gases and liquids. Its main part is a mechanical separator to separate the gaseous part from the liquid part, the second tank in which the separator is immersed, together with the water-cooling system, gas outlet section from the tank with a valve to gas pressure control in the upper part of the separator, pressure and temperature sensors at the condenser's outlet and, additionally, for CO_2 mass flow at the outlet of the separator.

The main task of the fifth sub-system is to provide necessary connections for motive water (with possible length adjustment and change of inlet diameter), water vapour and CO_2 inlet and outlet with the water/CO_2 mixture pressure control.

The last part of the whole test rig is responsible for measurement of necessary temperatures, pressures and flow rates in selected points together with data visualisation and recording for further processing and analysis. In addition, control of the selected parameters for process fluids should be possible.

The selection of proper measurement devices is very important from the point of view of the planned experiments. On the other hand, the variety of available solutions is a difficult task. Hence, the following sections will be discussed in more detail, taking into account the specifics of the presented installation.

2.2. Mathematical Description of SEC

The main task of the designed test facility is to provide the base for the spray ejector condenser investigation. Hence, the mathematical description of this element is needed to identify the measured physical quantities necessary to evaluate the performance of the analysed process. Its schematic view is given in Figure 2.

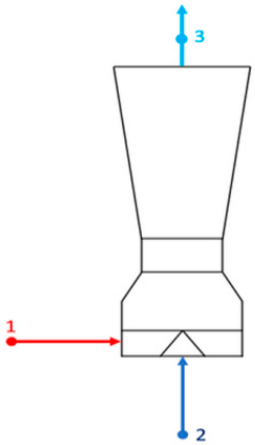

Figure 2. Scheme of spray-ejector condenser (1—suction fluid inlet, 2—motive fluid inlet, 3—outlet).

SEC has two inlets (for suction fluid and motive fluid) and one outlet. In case of water and steam SEC, according to energy balance, heat given by steam (suction fluid) is equal to heat absorbed by cooling water (motive fluid). From this, we obtain [34]:

$$\dot{Q}_s = \dot{Q}_{cw}, \tag{1}$$

and mass balance:

$$\dot{m}_s + \dot{m}_{cw} = \dot{m}_c. \tag{2}$$

When considering CO_2 added to suction fluid, then energy balance can be written in the following form:

$$\dot{Q}_{cw} = \dot{Q}_{vap\_C} + \dot{Q}_C + \dot{Q}_{cond\_c} + \dot{Q}_{CO2\_c}. \tag{3}$$

The cooling water draws heat from the cooling of the steam, cooling of CO_2, condensation of the steam and cooling of the condensed steam (water).

Heat of water vapour cooling $\dot{Q}_{vap\_C}$ is expressed as:

$$\dot{Q}_{vap\_C} = \dot{m}_{H_2O} \cdot (h_{1H_2O} - h_{sat\_vap}). \tag{4}$$

Heat of condensation Q_C was calculated according to the formula:

$$\dot{Q}_C = \dot{m}_{H_2O} \cdot r. \tag{5}$$

Heat of CO_2 cooling $\dot{Q}_{CO_2\_c}$ was calculated according to the formula

$$\dot{Q}_{CO_2\_c} = \dot{m}_{CO_2} \cdot (h_{1CO_2} - h_{3CO_2}). \tag{6}$$

Heat of water condensate cooling $\dot{Q}_{cond\_c}$ was calculated according to the formula:

$$\dot{Q}_{cond\_c} = \dot{m}_{H_2O} \cdot (h_{sat_{liq}} - h_{3H_2O}), \tag{7}$$

with:

$$h_{sat_{liq}} = h_{sat\_vap} - r. \tag{8}$$

Heat absorbed by cooling water can be expressed as:

$$\dot{Q}_{cw} = \dot{m}_{cw} C_w \cdot \Delta T. \quad (9)$$

Because the temperature of condensate is equal to cooling water temperature at the outlet, then:

$$\Delta T = T_c - T_{cw,in}. \quad (10)$$

The enthalpy of water vapour and liquid (h_{1H_2O}, h_{sat_vap}, r, $h_{sat_{liq}}$, h_{3H_2O}) can be obtained from IF-97 steam tables [35]. The enthalpy of carbon dioxide CO_2 (h_{1CO_2}, h_{3CO_2}) can be obtained from NIST tables [36].

As can be deduced from the above equations, for proper energy balance calculations, mass flow rate and temperature should be measured. Enthalpy is taken from various physical tables for given conditions defined by pressure and temperature. Hence, heat flows given in Equations (3)–(8) are measured indirectly.

When a given physical variable, y, is measured indirectly and is a function of independent measurements $x_1, x_2, \ldots, x_n$:

$$y = f(x_1, x_2, \ldots, x_n) \quad (11)$$

Using the propagation model of uncertainty [37–41], the standard combined uncertainty $u_c$of y can be calculated from the formula:

$$u_c(y) = \sqrt{\left(\frac{\partial y}{\partial x_1} u(x_1)\right)^2 + \left(\frac{\partial y}{\partial x_2} u(x_2)\right)^2 + \ldots + \left(\frac{\partial y}{\partial x_n} u(x_n)\right)^2}. \quad (12)$$

Then, the expanded uncertainty is calculated from the equation:

$$U = k\, u_c(y). \quad (13)$$

When considering Equation (4), it can be seen that the standard combined uncertainty can be written as:

$$u_c\left(\dot{Q}_{vap\_C}\right) = \sqrt{\left(\frac{\partial \dot{Q}_{vap\_C}}{\partial \dot{m}_{H_2O}} u\left(\dot{m}_{H_2O}\right)\right)^2 + \left(\frac{\partial \dot{Q}_{vap\_C}}{\partial h_{1H_2O}} u\left(h_{1H_2O}\right)\right)^2 + \left(\frac{\partial \dot{Q}_{vap\_C}}{\partial h_{sat\_vap}} u\left(h_{sat\_vap}\right)\right)^2} \quad (14)$$

with partial derivatives, as follows:

$$\frac{\partial \dot{Q}_{vap\_C}}{\partial \dot{m}_{H_2O}} = h_{1H_2O} - h_{sat\_vap}, \quad (15)$$

$$\frac{\partial \dot{Q}_{vap\_C}}{\partial h_{1H_2O}} = \dot{m}_{H_2O}, \quad (16)$$

$$\frac{\partial \dot{Q}_{vap\_C}}{\partial h_{sat\_vap}} = \dot{m}_{H_2O}. \quad (17)$$

Uncertainty of mass flow rate measurement, $u\left(\dot{m}_{H_2O}\right)$, can be easily estimated based on the manufacturer's data for a given device. The uncertainty concerning water enthalpy, and also saturated vapour, depends on estimation accuracy of this variable. According to IF-97 and NIST tables, within the region of interest, the enthalpy of steam is defined at a given temperature and pressure with the uncertainty of ±0.2% [42]. The specific enthalpy of CO_2 is provided with an uncertainty of 0.95% [43].

However, if indirect measurements are used, then enthalpy is estimated based on measured temperature and pressure. Then, the total uncertainty of its estimation should be calculated from the relationship:

$$u(h) = \sqrt{(u_{h,table})^2 + (u(p))^2 + (u(T))^2}, \quad (18)$$

For the next element of heat balance, heat of condensation, given by Equation (5), it can be written:

$$u_c\left(\dot{Q}_C\right) = \sqrt{\left(\frac{\partial \dot{Q}_C}{\partial \dot{m}_{H_2O}} u\left(\dot{m}_{H_2O}\right)\right)^2 + \left(\frac{\partial \dot{Q}_v}{\partial r} u(r)\right)^2} \quad (19)$$

and with the following partial derivatives:

$$\frac{\partial \dot{Q}_C}{\partial \dot{m}_{H_2O}} = r, \quad (20)$$

$$\frac{\partial \dot{Q}_C}{\partial r} = \dot{m}_{H_2O}. \quad (21)$$

The calculation of uncertainty for heat of CO_2 cooling, $\dot{Q}_{CO2\_c}$, and heat of water condensate cooling, $\dot{Q}_{cond\_c}$, results in equations in the same form as for heat of water vapour cooling, $\dot{Q}_{vap\_C}$. Hence, this procedure is not presented here.

For the next element, heat absorbed by cooling water, we obtain:

$$u_c\left(\dot{Q}_{cw}\right) = \sqrt{\left(\frac{\partial \dot{Q}_{cw}}{\partial \dot{m}_{cw}} u\left(\dot{m}_{H_2O}\right)\right)^2 + \left(\frac{\partial \dot{Q}_{Cw}}{\partial C_w} u(C_w)\right)^2 + \left(\frac{\partial \dot{Q}_{cw}}{\partial \Delta T} u(\Delta T)\right)^2} \quad (22)$$

with:

$$\frac{\partial \dot{Q}_{cw}}{\partial \dot{m}_{cw}} = C_w \cdot \Delta T, \quad (23)$$

$$\frac{\partial \dot{Q}_{cw}}{\partial c_w} = \dot{m}_{cw} \cdot \Delta T, \quad (24)$$

$$\frac{\partial \dot{Q}_{cw}}{\partial \Delta T} = \dot{m}_{cw} C_w. \quad (25)$$

Taking into account Equation (9), it should be noted here that:

$$u_c(\Delta T) = \sqrt{\left(\frac{\partial \Delta T}{\partial T_c} u(T_c)\right)^2 + \left(\frac{\partial \Delta T}{\partial T_{cw,in}} u(T_{cw,in})\right)^2}, \quad (26)$$

with:

$$\frac{\partial \Delta T}{\partial T_c} = 1, \quad (27)$$

$$\frac{\partial \Delta T}{\partial T_{cw,in}} = -1. \quad (28)$$

Using presented relationships, there can be estimated measurement uncertainties at given known operating conditions.

2.3. Design Assumptions

The input assumptions for the technical analysis and selection of measurement equipment were taken from the simulation model of the considered cycle (Figure 1). At first,

rated values were assumed as follows: water inlet at 17 °C and 12 bar, gas inlet at 150 °C, 0.2/0.9 bar and 0.01 kg/s. Outlet pressure was established at 1.10/1.15 bar. These operating parameters are the result of the first stage of the condenser design. It should be then experimentally tested.Hence, at the first stage of simulations, it was established that the designed system has to allow for adjustment of the operating parameters in the range presented in Table 1.

Table 1. The range of operating variables.

Location	Temperature	Pressure	Mass Flow
	°C	bar	kg/s
Water inlet	5–20	2–16	Resulting
Gas inlet	110–170	0.2–2.0	0.008–0.015
Outlet	Resulting	1–3	Resulting

In the next step, detailed simulations were performed to establish operating conditions in both extreme (minimum/maximum) cases representing two variants of the condenser operation (gas pressure at the inlet 0.2 bar and 0.9 bar). Table 2 summarises the selected values in the most important points of the designed test rig.

Table 2. Simulated values of operating variables in two variants.

Variable	Variant 1	Variant 2
Steam/CO_2 mixture pressure at the inlet to SEC	0.9 bar	0.2 bar
Steam flow rate at the inlet of SEC	8 g/s	8 g/s
CO_2 flow rate at the inlet to SEC	2 g/s	2 g/s
Motive water flow rate at the inlet to SEC	340 g/s	4399 g/s
Mixture flow rate at the outlet of SEC	350 g/s	4409 g/s
Motive water temperature at the inlet to SEC	17.0 °C	17.0 °C
Average mixture temperature at the outlet of SEC	32.2 °C	18.4 °C
CO_2 temperature before mixing valve with steam	70.0 °C	70.0 °C
Steam temperature before mixing valve with CO_2	161.0 °C	161.0 °C
Steam/CO_2 mixture temperature at the inlet to SEC	151.2 °C	151.2 °C
Mass Entrainment Ratio	0.0294	0.0023
Volumetric Entrainment Ratio	56.38	19.62

The presented values set the operating conditions for further selection of the measurement equipment. For practical reasons,it was additionally assumed that the mass flow rate of steam, CO_2 and motive water can be controlled from zero to approximately 120% of the maximum values. This creates a safety margin for flow meters, especially those sensitive to exceeding rated operating conditions. Based on this, and taking into account the physical side of the considered phenomena, there were established borders defining the variability of basic thermodynamic parameters in the considered points (Table 3).

Table 3. Variability ranges of measured quantities in selected points.

Process Fluid	Temperature Range	Pressure Range	Mass Flow Rate Range	Desired Accuracy
	°C	bar	g/s	% mol
CO_2	20–70	1–1.5	0–2	–
Steam	100–170	1–1.5	0–8	–
CO_2 + steam	110–170	1–1.5	0–10	–
Water	10–20	10–12	0–6000	–
Water + CO_2 (dissolved)	15–30	1–1.5	0–6000	0.0.1–0.1

2.4. Selected Design Aspects

The design of the test rig depends on the selected specific solutions and technical requirements of manufacturers. Hence, at this stage, it is difficult to provide detailed considerations. For these reasons, the procedure to estimate pressure loss in a water supplying system (system III in Figure 1) is presented, which is crucial for selection of a pump.

We begin with calculations of hydraulic loss. The pipe diameter was set at DN 50 and, following Table 2, the two extreme values of the mass flow rate Q_{min} = 340 g/s and Q_{max} = 4399 g/s were assumed. The cross-sectional area for solution flow was for the diameter DN 50: $A_{50} = 2.04 \times 10^{-3} m^2$. Hence, the minimum and maximum flow velocity are: w_{d50min} = 0.17 m/s and w_{d50max} = 2.16 m/s, respectively.

Then, the friction factor to obtain major (friction) losses in a pipe was determined. The Reynolds number was computed from the definitional relationship:

$$\mathrm{Re} = \frac{w_r \cdot d}{\nu_r}. \tag{29}$$

The kinematic viscosity for water is $\nu_r = 9.79 \times 10^{-7}$ m^2/s.

For the diameter DN 50, we obtain:

$$\mathrm{Re}_{50min} = \frac{0.17 \times 0.051}{0.000000979} = 8856, \tag{30}$$

$$\mathrm{Re}_{50max} = \frac{2.16 \times 0.051}{0.000000979} = 112523. \tag{31}$$

The friction factor of major losses, λ, was calculated from the Nikuradse formula:

$$\frac{1}{\sqrt{\lambda}} = 2\log\left(\frac{D}{k} + 1.14\right). \tag{32}$$

where:

k—average roughness of the pipeline; for new pipes k = 0.02–0.10 mm.

It was assumed that k = 0.008 mm. From the above, for the diameter DN = 50 mm, the average friction factor λ = 0.241.

The pressure loss in a straight pipe section is given by the Darcy–Weisbach formula:

$$\Delta p_l = \lambda_{50} \frac{1}{d_{50}} \cdot \frac{\rho w^2}{2}. \tag{33}$$

The pressure loss per unit length of a straight pipe of 1 m length is:

$$\Delta p_{50/m} = \lambda_{50} \frac{1}{d_{50}} \cdot \frac{\rho w^2}{2}. \tag{34}$$

From the above: $\Delta p_{50/m\,max}$ = 11010 Pa/m and $\Delta p_{50/m\,min}$ = 68 Pa/m.

Based on the initial design, the total length of the straight pipe sections was assumed to be L = 12 m. From Equation (37) and for DN = 50 mm, we obtain Δp_{50Lmin}= 816.0 Pa and Δp_{50Lmax} = 132.12 kPa.

Minor pressure losses are a consequence of the presence of elements disturbing the flow in the pipeline-elbows, fittings, etc. Accurate determination of the value of these losses requires precise knowledge of the flow characteristics of these elements.

When changing the flow direction, the local resistance coefficient can be determined from the relationship:

$$\xi, = 0.946 \sin^2\left(\frac{90}{2}\right) + 2.05 \sin^4\left(\frac{90}{2}\right). \tag{35}$$

When changing the flow direction by 90°, the local resistance coefficient has the value ξ = 0.9855, and the minor pressure loss is given by the relationship:

$$\Delta p_m = \xi \frac{\rho w^2}{2}. \quad (36)$$

From Equation (40) for the DN50 diameter, we obtain: $\Delta p_{50/\xi,\,min}$ = 14 Pa, $\Delta p_{50/\xi,\,max}$ = 2299 Pa. The change of direction at an angle of 90° in the system will take place n = 3 times, then the total minor losses. Hence, $\Delta p_{\xi,50\ min}$ = 42 Pa and $\Delta p_{\xi,50\ max}$ = 6.897 kPa.

The remaining local resistances resulting from the installed fittings and instrumentation were replaced with the equivalent linear resistances, assuming the equivalent length L_Z = 5 m. For the equivalent length, we determined the values of minor pressure losses.

For the DN50 diameter, we obtain:

$$\Delta p_{50Z} = \Delta p_{50/m} \cdot L_Z. \quad (37)$$

From Equation (40): Δp_{50zmin} = 68 Pa/m × 5 m = 340 Pa and Δp_{50zmax} = 11.01 kPa/m × 5 m = 55.05 kPa.

The total minor losses in the system are the sum of the bend losses and the equivalent minor losses:

$$\Delta p_{50m} = \Delta p_{50Z} + \Delta p_{\xi,50}. \quad (38)$$

From the above, we obtain Δp_{50mmin} = 340 + 42 = 382 Pa and Δp_{50mmax} = 55.05 + 6.897 = 61.95 kPa.

Total pressure in the pipeline is the sum of minor and major pressure losses:

$$\Delta p_r = \Delta p_L + \Delta p_m. \quad (39)$$

Its minimum and maximum values are then Δp_{50rmin}= 816 + 382 = 1.2k Pa and Δp_{50rmax} = 132.12 + 61.95 = 194.07 kPa, respectively. Hence, the total maximum pressure loss was assumed to be 194.1 kPa, and this value was used to select the water pump.

3. Selection of Measurement Techniques and Devices

3.1. Temperature

Temperature measurement is very important in numerous technical, industrial and scientific applications. The accuracy of a performed measurement depends on technical and physical factors and relies on the proper selection of the measuring method and device. This is influenced by the kind of medium and the dynamics of physical phenomena occurring within the studied area. They can be defined before the measurements are carried out. Depending on the amount of input design data, there can be defined measurement conditions necessary for the choice of the appropriate measurement method and tools. Due to the use of heat transfer mechanisms, two kinds of temperature measurement methods are defined, i.e., contacting or non-contacting methods [44].

As far as the designed test bed is concerned, the temperature range of working mediums is from 10 °C to 180 °C. Hence, both contact and non-contact methods can be applied here. For practical reasons, contact methods applying thermocouples (TC) and resistance temperature detectors (RTD) are the most useful. This is because both these kinds of sensors provide electrical-type output measurement signals, which can be very easily transmitted and converted in computer measurement systems [45].

Depending on the kind of the resistive material used, currently, RTDs are manufactured in three variants, namely, as copper, nickel or platinum resistors. The use of the first two is typically restricted to the range from −50 °C to +160 °C. The most popular are platinum sensors due to their good accuracy, low cost and reproducibility. Their application covers the range from −200 °C to +850 °C. Thin-film resistors can be very small with the length of 3 mm. They also offer high accuracy. Following the IEC 60751 standard [46], at a temperature of 200 °C, the wire-wound A-class sensor has the tolerance of ±0.44 °C. However, the platinum resistive wire is completely encapsulated to avoid a negative

external environment (mechanical stress, corrosion, oxidation, etc.). However, it results in poorer long-term stability and large hysteresis due to differences in thermal expansion of the substrate and the wire and the indirect contact of the wire and process medium [47]. This effect is enhanced when placing the encapsulated sensor in a protective sheath.

The operation of thermocouples is based on Seebeck's thermoelectric effect. They offer significantly wider measurement range, from −270 °C to +1370 °C (K-type nickel–chromium alloy thermocouple) to over 2000 °C (Pt-Rh thermocouples). Tolerance classes are given in IEC 60584 [48], and for class 1 of a sensor at a temperature of 200 °C,the tolerance is from ±0.50 °C (type T) to ±1.50 °C (types E, J, K and N).

The sensitive measuring point of the thermocouple is the measuring junction, where the electrical and thermal contact between two conductors. As this junction can be very small (diameter below 0.5 mm), thermocouples may offer low short response time and are better suited to measurements when thermal dynamics are of greater importance. This type of junction is called exposed. However, to protect against the negative impact of the external environment, a junction is mounted in a suitable protective tube, also named a well or sheath. In such a case, a junction can be mounted in two variants. The first one is ungrounded, a junction suspended inside the metallic sheath, such that the junction is not in contact with the sheath. It causes the thermocouple to react to the temperature change in the environment longer because the sheath must reach thermal equilibrium before the junction can detect that change. In the second one, with a grounded junction, a junction is welded to the inside of the sheath resulting in a shorter reaction time to temperature changes.

To clarify this issue, in Table 4, on the base of manufacturers catalogues [49], the time after which the sensor's response to a step change in temperature reaches 90% of its maximum value in case of isolated and grounded thermocouples in moving water (0.4 m/s) and air (2 m/s)is given.For comparison, the same parameter was also given for RTD sensors of the same manufacturer in the same flow conditions in Table 5. It is clearly visible that they have a longer response time. Hence, this parameter should be balanced with accuracy when considering applications requiring more precise dynamic process analysis.

Table 4. The time after which the thermocouple's response to a step change in temperature reaches 90% of its maximum value, s.

Sheath Diameter/Junction Type	Water 0.4 m/s	Air 1 m/s
1 mm/grounded	0.18	10
1 mm/insulated	0.50	10
3 mm/grounded	0.75	80
3 mm/insulated	2.90	88
6 mm grounded	2.60	185
6 mm/insulated	9.60	200
8 mm/grounded	3.90	250
8 mm/insulated	14.00	290

Table 5. The time after which the RTD's response to a step change in temperature reaches 90% of its maximum value, s. Steel sheath.

External Diameter and Wall Thickness, mm	Water 0.4 m/s	Air 1 m/s
6 × 0.5	55	260
10 × 1.5	100	400
15 × 1.5	170	490
22 × 2.0	480	1200

The maximum process fluid velocity is 8.9 m/s, 18.5 m/s, 24.8 m/s and 3.3 m/s for CO_2, steam, steam + CO_2 and water, respectively. These values guarantee that the thermal time constant should decrease by over 3–4 times in relation to still air or water [50].

The most important advantages of RTDs are: good accuracy, stability, sensitivity and reproducibility. On the other hand, they are more expensive, larger and more fragile than thermocouples.

It should also be noted that when an RTD insulation resistance is affected by moisture, an additional error is introduced. Hence, Pt100 sensors offer better long-term stability when compared to Pt1000. At the same time, the resistance of lead wires should be taken into account, and for this reason, 4-wire and 3-wire measurement circuits are preferred.

Thermocouples are relatively inexpensive, manufactured in a variety of sizes and cover a wide temperature range. They are smaller than RTDs, reasonably stable, reproducible and fast. Additionally,thermoelectric force is independent of wire length and diameter.

The low output signal from TCs is sensitive to electrical noise and requires additional amplifiers. Furthermore, bare thermocouples cannot be used in conductive fluids, and the thermoelectric junction is sensitive to stress and vibration.

In the designed test rig,the ambient temperature should not exceed the typical values of 20–30 °C met in indoor conditions. Therefore, its impact on thermal conditions of the rig can be omitted. Research on SEC operation is planned to be conducted in thermally established conditions. Gas, steam and water flows in piping are supposed to be well developed. The distance between the data logger and measuring points (length of lead wires) should not exceed 3 m. Hence, A-class Pt100 sensors were chosen for temperature measurements.

3.2. Pressure

Piezoelectric transducers are commonly used among commercially available electric pressure transducers due to their accuracy, stability, linearity and favourable price. To reduce temperature errors, the elastic element (membrane) should be protected against the action of the high-temperature fluid. Hence, in the considered test rig selection, pressure sensors should be based not only on the expected pressure values but on the maximum temperature of process fluid.

In case of process temperatures over 200 °C,a non-insulated siphon tube is usually installed between the process connection and the pressure sensor. In that tube, condensate or chilled water accumulates, protecting the elastic element against high fluid temperature. Its length depends on the process temperature and maximum working temperature of the pressure sensor.

It may be sufficient to use the special finned cooling element in applications for lower process temperatures, usually with 3 or 5 fins.

3.3. Flow Rate

As given in Section 2, four measuring points were selected: CO_2, steam, steam + CO_2 and motive water. A two-phase flow is not meant to occur. Only in one case will a mixture of gases flow. Temperature and pressure conditions are given in Table 2.

Mass flow rate measurement is more convenient than volume flow from the point of view of energy balance equations in thermodynamic systems. However, both mass and volume flow measurement methods and devices are considered in this paragraph because all of them have certain advantages that can be decisive when choosing a given solution.

The operation of differential pressure flow meters (orifice plate, Venturi tube, and nozzle) is based on Bernoulli's equation. They are simple and reliable devices when manufactured and installed following relevant standards. Their main disadvantage is pressure drop and their sensitivity to installation conditions. They are commonly used in fluids and dry gases mass flow measurements. In case of two-phase flows, a broad range of empirical models were developed to correlate mass flow rate with pressure drop for different types of flow and fluid combinations.

Table 6 presents selected results for the design of orifice flow meters for the considered four points following ISO/TR 15377:2007 and EN ISO 5167:2005 standards. In all cases, a single 90° elbow or tee (single branch flow) at the inlet of the meter was assumed. Pressure drop is given at maximum mass flow.

Table 6. Selected parameters of orifice plates.

Process Fluid	Inlet Length	Outlet Length	Minimum Flow	Maximum Flow	Pressure Loss
	m	M	kg/s	kg/s	kPa
CO_2	0.56	0.22	0.000	0.003	0.135
Steam	1.20	0.20	0.002	0.015	1.861
CO_2 + steam	1.20	0.20	0.002	0.015	1.861
Water	2.40	0.43	0.219	6.000	9.050

Among variable area flow meters, rotameters are very popular because of their simple and reliable construction, low pressure drop and applicability to various clean gases and liquids, because sediments and gas bubbles affect accuracy. For gases, the effect of pressure and temperature is taken into account using scale correction factors. Typical accuracy is 1 to 4% of the full scale.

The main part of a turbine flow meter is a turbine rotor. It is concentrically mounted on a shaft in a pipe with a measured flow Rotation velocity rate depends on fluid volume passing in a given time step. The typical accuracy is 0.25%.

The operation of the electromagnetic flow meters is based on Faraday's law of electromagnetic induction. When the conductive liquid passes through a channel or a pipe, an electromotive force (voltage) is induced and measured by two electrodes mounted flush to the pipe wall. This voltage depends proportionally on the average flow velocity (and volume flow rate). Because the measured medium must be conductive, that type of flow meter is not suitable for gas flow. Typical accuracy can be 0.5% to 1%, but it can be worsened by impurities in the liquids.

Ultrasonic flow meters can be applied in a broad range of fluids providing no obstruction to flow. Two types are in use: Doppler and transit time.

In the Doppler flow meter, pulses of high-frequency sound waves are sent across the pipe and then received by the detector. The wave moving with the flow travels faster than that moving against the flow. The time difference between these two periods depends on the fluid flow rate. Hence, this kind of ultrasonic flow meter requires clean fluids for proper operation because sound waves are reflected or scattered from suspensions in the flow path.

The transit time flow meter measures the time difference between two ultrasonic pulses transmitted against and with the flow. This device is also sensitive to entrained gas bubbles and solid particles.

The operation of vortex flow meters is based on the Karman vortex streets phenomenon. The main advantage of this meter is the independence of measured volumetric flow on the fluid density, simple construction, lack of moving parts and good operation with liquids and gases, but it creates a pressure drop comparable to the orifice plate or turbine meters. Typically, it has 1% accuracy.

Coriolis flow meters directly measure the mass flow of fluids of different densities and viscosities. They can also measure the mass flow of two-phase mixtures, liquid–liquid (such as emulsions) and liquid–solid [51].

Their principle of operation is based on the use of the Coriolis phenomenon, which causes the occurrence of inertial forces in the case of simultaneous rotational and progressive motion of the body. The direction of the inertia force is determined by the vector product of the linear velocity and the rotational speed. In flow meters using this phenomenon, the rotational motion was replaced by the vibrating motion of the measuring tubes. The measure of the mass flux is the value of the phase shift of vibrations at the inlet and outlet of these tubes (often two are used).

Thermal flow meters utilise the principle that the rate of heat absorbed by a flowing fluid is proportional to its mass flow rate.

Two types of thermal mass meters are in use: constant temperature and constant current. In the first case, the temperature rise (which depends on the mass flow) of the

flowing fluid is measured at a fixed heat transfer rate. In the second case for a fixed temperature rise, the heat transfer rate is measured. Its value increases with the fluid mass flowrate. These devices can be used for liquid flows, but practically,they are used mainly for gas flow measurements. Their typical accuracy is 2%.

In order to choose reliable devices among commercially available devices while considering economical and technical constraints, a more detailed analysis was performed. First, questionnaires were sent with operational conditions for selected measuring points to the several leading manufacturers. The obtained answers formed the basis for further considerations.

As given in Table 7, the most economically competitive solution is an orifice flow meter. They are simple and reliable, but additional measurements of fluid pressure and temperature should be performed to measure mass flow. Coriolis mass flow meters provide a reliable measurement but are the most expensive. Hence, other factors were taken into account.

Table 7. Types and prices (EUR net, 04.2022) of flow meters proposed by different suppliers.

Process Fluid	1	2	3	4
CO_2	Orifice/990	Thermal [1]/3900	Coriolis [1]/4900	Rotameter/1500
Steam	Orifice/835	Vortex [1]/3000	Coriolis [1]/4000	Vortex/2500
CO_2 + steam	Orifice/835	Vortex/2100	Coriolis [1]/4000	Vortex/2500
Water	Orifice/875	Electromagnetic/1750	Coriolis [1]/9800	Coriolis [1]/5800

[1] Mass flow measurement.

Table 8 shows the declared accuracy of all devices. In all cases, the presented values include the total accuracy including the error of the volume/mass flow transducer and the electronic converter. The Coriolis flow meters offer the best accuracy in mass flow measurements but are also expensive. An interesting option for CO_2 is the thermal mass flow meter.

Table 8. Maximum errors of studied solutions at rated flow, %.

Process Fluid	1	2	3	4
CO_2	0.85	1.00	0.50	1.60
Steam	1.32	1.10	0.10	1.50
CO_2 + steam	1.32	1.10	0.10	1.50
Water	0.92	0.53	0.10	0.15

The next parameter to be considered is pressure loss. Its value affects flow conditions and must be considered when choosing a circulating pump or the place where pressure transducers will be installed. Its maximum values are given in Figure 3. The fourth supplier did not provide the information about pressure loss for water flow measurement. In the case of the second manufacturer, the proposed electromagnetic device has no pressure loss.

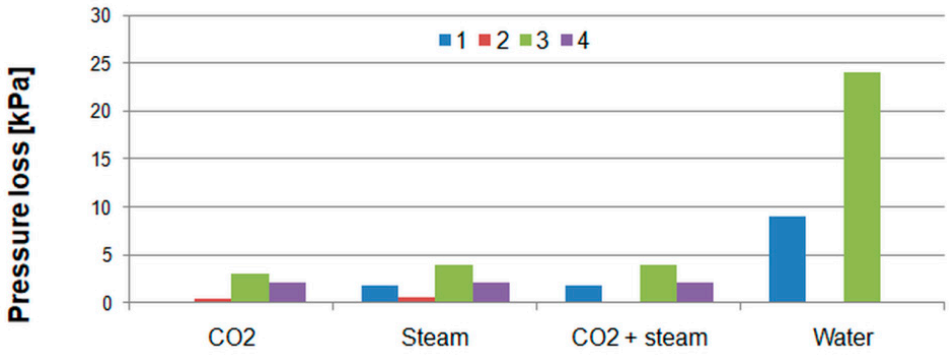

Figure 3. Maximum pressure loss at rated flow.

Table 9 shows selected solutions. The second solution was evaluated as the most competitive. The thermal flow meter for CO_2 was selected because of this reasonable price and good quality. For steam measurement, the vortex mass flow meter was chosen. In the final case, motive water, the electromagnetic device was selected. It measures volume flow. However, as motive water temperature is supposed to vary within a narrow range, the mass flow rate can be easily and precisely measured from volume flow rate and water temperature. It is also very important that this type of flow meter has negligible pressure loss in relation to other solutions: 24 kPa for the Coriolis flow meter and 9.05 kPa for the orifice meter, which significantly impacts pump selection and operation.

Table 9. Selected parameters of chosen solutions.

Process Fluid	Type	Minimum Flow	Maximum Flow	Pressure Loss
		kg/s	kg/s	kPa
CO_2	Thermal	0.0005	0.002	0.05
Steam	Vortex	0.005	0.013	0.67
CO_2 + steam	Vortex	0.005	0.010	0.40
Water	Electromagnetic	0.100	6.000	0.00

3.4. CO_2 Content

The measurement of CO_2 content, both dissolved in water and gaseous in air, is technically demanding due to this gas's physical and chemical properties. Several methods are currently in use in technical applications.

On the base of the conducted literature review [52–54] several CO_2 sensors were selected that possibly would be applicable in the designed test rig. They are as follows:

- Potentiometric sensors—Severinghaus,
- Potentiometric sensors—Solid electrolyte sensors,
- Non-dispersive infrared (NDIR) CO_2 sensors.

The main disadvantage of the potentiometric sensor is the necessary calibration procedure before measurements. It is difficult if measurements must be carried out under field conditions or for solutions with unknown and changing composition. Their typical response time is between 30 s and 120 s. The operation temperature is up to 50 °C.

Solid electrolyte sensors are, in principle, similar to the abovementioned. The operational temperature is usually within the 200–750 °C range. For semiconductor sensors, it is from −10 to 100 °C. Additional external power is required to heat up the sensor. The output of the electrical signal depends on gas concentration. Typical response time is approximately 1 s. These sensors do not require calibration but can be used only in gas applications.

The operation of the non-dispersive infrared (NDIR) sensors is based on the concentration-dependent absorption of electromagnetic radiation in the IR range. Their response time is usually between 5–30 s. Modern solutions are equipped with in-built converters and self-calibration functions. A short comparison of these sensors is given in Table 10.

Table 10. Selected parameters of CO_2 concentration measurement sensors.

Type	Response Time T0.9	Operating Temperature	Calibration	External Power
	s	°C	-	-
Severinghaus	30–120	<50	Yes	No
Solid electrolyte	<1	30–120	No	Yes
NDIR	5–30	0–50	No	Yes

On the basis of the presented review, recommended solutions were chosen. Three possible measurement points in the designed test rig were selected:

- CO_2 dissolved in outlet water from SEC,

- gaseous CO_2 at the outlet from the separator,
- CO_2 inside SEC.

For the first point, the Severinghaus-type potentiometric sensor can be recommended. Despite a troublesome initial calibration procedure, it can be used, as there are assumed stable operating conditions. However, the minimum response time should be thoroughly checked at first. The concentration of gaseous CO_2 can be easily determined using an NDIR sensor [53]. In the last case, inside SEC, a currently commercially available solution at a reasonable price cannot be proposed.

3.5. Data Acquisition

As the data acquisition system, a device with simultaneous sampling of measured inputs should be used. The possible solution should allow data recording with time stamps from approximately 0.1–1 s to 10 min.

The type of analogue measurement signals is of secondary importance. Typical output signals from sensors are recommended, both in voltage (0–10 V) or in current (4–20 mA) standards. The latter is safer from a practical perspective, because zero current means failure occurred in the circuit. In the case of voltage standard, this state can be interpreted as zero value of the measured quantity or as a fault in the system.

Temperature sensors require additional temperature converters. Pressure transducers have in-built converters. Flow meters are usually equipped with current (4–20 mA) and pulse/frequency outputs proportional to the value of the measured quantity.

4. Results and Discussion

Following the design assumptions presented in previous sections, input parameters for uncertainty calculations were chosen. They are given in Figure 1 and Table 2 as Variant 1. Based on these parameters, the thermodynamic parameters of water, steam and CO_2 in characteristic points of a spray ejector condenser are given in Table 11.

Table 11. Thermodynamic parameters of water, steam and CO_2 in characteristic points of a spray ejector condenser.

Variable	1	2	3
T [°C]	151.16	17.0	32.23
p [bar]	1.50	12.0	1.22
h_{H2O} [kJ/kg]	2775.25	72.50	135.16
h_{CO2} [kJ/kg]	620.18	-	511.83

In addition, from NIST tables, p = 1.50 bar: h_{satvap} = 2693.13 kJ/kg, h_{satliq} = 467.0807 kJ/kg and r = 2226.033 kJ/kg were estimated.

As the full uncertainty analysis, presented in Section 2.3, is too complicated to be presented here for all possible variants and variables, we presented an analysis for heat flux from water vapour cooling.

Taking values from Table 11, Equations (15)–(17) provide results as follows:

$$\frac{\partial \dot{Q}_{vap\_C}}{\partial \dot{m}_{H_2O}} = 2775.25 - 2693.13 = 82.19 \frac{kJ}{kg}, \tag{40}$$

$$\frac{\partial \dot{Q}_{vap\_C}}{\partial h_{1H_2O}} = 0.008 \frac{kg}{s}, \tag{41}$$

$$\frac{\partial \dot{Q}_{vap\_C}}{\partial h_{sat\_vap}} = 0.008 \frac{kg}{s}. \tag{42}$$

The uncertainty of the mass flow measurement, $u(\dot{m}_{H_2O})$, can be taken directly from the manufacturer's datasheet and depends on the chosen device.

Taking the uncertainty of the steam enthalpy estimation as 0.2% (see Section 2.2), we obtain:

$$u(h_{1H_2O}) = 2775.25 \times \frac{0.2}{100} = 5.55 \frac{kJ}{kg}. \quad (43)$$

Taking the uncertainty of the steam enthalpy estimation as 0.2% (see Section 2.2), the accuracy of pressure measurement as 0.5% and temperature as 0.1% for h_{sat_vap} = 2693.13 kJ/kg, we obtain from Equation (18):

$$u(h_{sat\_vap}) = \sqrt{(u_{h,table})^2 + (u(p))^2 + (u(T))^2} = 14.75 \frac{kJ}{kg}. \quad (44)$$

Assuming the uncertainty of mass flow measurement $u(\dot{m}_{H_2O}) = 0.1\%$ and substituting the obtained values in Equation (19), we obtain:

$$\frac{\partial \dot{Q}_{vap\_C}}{\partial \dot{m}_{H_2O}} u(\dot{m}_{H_2O}) = 8.219 \text{ kg/s}, \quad (45)$$

$$\frac{\partial \dot{Q}_{vap\_C}}{\partial h_{1H_2O}} u(h_{1H_2O}) = 44.404 \text{ kg/s}, \quad (46)$$

$$\frac{\partial \dot{Q}_{vap\_C}}{\partial h_{sat\_vap}} u(h_{sat\_vap}) = 118.006 \text{ kg/s}, \quad (47)$$

and:

$$u_c\left(\dot{Q}_{vap\_C}\right) = \sqrt{(8.219)^2 + (44.404)^2 + (118.006)^2} = 126.35 \text{ W} \quad (48)$$

In the same way, $u_c\left(\dot{Q}_{vap\_C}\right)$ from Equation (19) can be computed. The results for the various considered flow meters were as follows: 126.33 W, 126.31 W, 126.09 W and 126.77 W for orifice, first vortex, Coriolis and second vortex flow meters, respectively.

Several authors presented their concepts of test rigs with direct contact heat exchangers. The most important findings related to measurement devices are presented in the following paragraphs.

In test rigs with direct contact condensers for the temperature measurement of process fluids, both thermocouples and resistance sensors were used. In the first group, various types were chosen. The most popular was the K-type (nickel–chromium/nickel–alumel) thermocouple with a typical uncertainty of ±1.5 °C, within the range from −40 °C to 1000 °C [55,56]. However, sometimes authors used specially calibrated thermocouples to obtain better accuracy, as of ±1 °C [57,58], ±0.2 K in the range of 0–600 °C [59], 0.5% within the range 0 °C–200 °C [60] or of 0.1% [61] at the same conditions.

The latter group of sensors was represented mainly by Pt100 sensors [62] with typical accuracy of ±0.1 °C [63–65].

However, authors did not provide any further details on selection procedure to choose the given type of sensor in certain application.

For pressure measurement, mainly piezoresistive absolute and differential pressure transducers were used, with an uncertainty of 2% at temperatures up to 50 °C or 4% up to 80 °C [55,56], ±0.5% of full-scale (FS) with a measurement range of 0–25 MPa [66] or of 0.1% FS and range from 200 to 700 kPa [67]. The accuracy of the sensors in high temperature steam measurements was reported as 0.1% (0–1 MPa) [60] or 0.2% (0–1.6 MPa) [59].

When analysing published studies, the flow measurements of water and steam involved the application of a large variety of techniques, from classical methods to modern electronic devices. Genić et al. [63] applied orifice flow meters (meeting ISO 5167-1 requirements) with mercury U-tube manometers. In the case of water flow measurement, however,

electromagnetic and turbine flow meters prevailed (Table 12). When steam flow rate is considered, vortex flow meters were the most popular (Table 13). However, despite a wide range of analysed studies, no selection guidelines were given by the authors.

Table 12. Devices used in water flow measurements.

Type	Range	Error	Reference
Rotameter	1–7 m^3/h	0.1 m^3/h	[68]
Electromagnetic	0.08–2.78 kg/s	0.2%	[60]
Electromagnetic	0.88–17.66 m^3/h	0.5%	[59]
Electromagnetic	0–10 m^3/h	1.0%	[66]
Rotameter	-	1.25%	[58]
Electromagnetic	0–30 m^3/h	0.5%	[28]
Turbine	0.04–0.25 m^3/h	1.0%	[59]
Turbine	0.6–6 m^3/h	1.0%	[59]
Rotameter	1–10 m^3/h	1.5%	[59]
Turbine	0.9–13.6 m^3/h	0.15%	[59]

Table 13. Devices used in steam flow measurements.

Type	Range	Error	Reference
Orifice	-	1.0 Pa	[68]
Vortex	7.5–73.9 g/s	1.0%	[60]
Vortex	30 to 300 m^3/h	1.5%	[59]
Vortex	0–40 m^3/h	0.75%	[28]
Vortex	0–120 m^3/h	0.75%	[28]
Vortex	0–150 kg/h	1.0%	[59]
Vortex	-	2.0%	[64]
Orifice	-	1.5%	[64]

Some authors also applied flow visualisation techniques. For example, Zong et al. [69] presented an experimental study on the direct contact condensation of steam jet in sub-cooled water flow in a rectangular mix chamber.

The steam and water temperature were measured by the K-type thermocouples (diameter of 1 mm, measurement range of 0–200 °C) with a maximum error of 0.5%. The 0–1 MPa, high-temperature pressure transducers with maximum error of 0.1% were used. A vortex flow meter with the range of 2700–26,600 kg/h and a maximum error of 1.0% was used for steam flow rate measurements. Additionally, a 330 kW electric steam generator with a maximum capacity of 0.11 kg/s was used as a steam source. The steam flow rate was controlled manually by a valve. The water flow rate was measured by an electromagnetic flow meter of 290–10,000 kg/h with a maximum error of 0.2%. The water flow rate was controlled by valves on feeding and bypass lines.

To record and visualise the flow field of the direct contact condenser, the Phantom V611 type high-speed camera, with 5 kHz frequency, was used. The LabVIEW data acquisition system, including an industrial computer, a National Instruments cDAQ-9178 data acquisition module, two NI 9213 modules (for temperature sensors)and four NI 9203 modules (for pressure transducers)were used.

The presented cases reveal a variety of used measuring devices. Thermocouples were usually used in temperature measurements due to their low thermal time constant. The piezoelectric transducer is a common solution in pressure measurement. Flow rate is the most problematic, and it should be noted here that applied solutions depend not only on the technical requirements but also on economic factors.

5. Conclusions

The presented concept of the laboratory test rig to experimentally investigate an application of a spray condenser in a CO_2 capture system in a thermal power plant cycle

is novel and requires an in-depth analysis of the available sources in terms of the proper selection of measurement equipment.

The indicated solutions were chosen based on detailed simulations in a well-established environment. The provided results were then used as boundary conditions to choose the measurement equipment.

This part of the design procedure is very problematic as various technical and economic factors should be taken into account. However, comparison with other works showed that the manual control of process parameters is sufficient during operation of the studied cases, and stable thermal conditions were easily achieved. For these reasons, the dynamic phenomenon can be treated as less important, and more attention can be given to the analysis of the steady states, which are the normal operating states of thermal power plants.

Author Contributions: Conceptualization, P.M. (Paweł Madejski) and K.B.; methodology, P.M. (Paweł Madejski), P.M. (Piotr Michalak), M.K. and K.B.; software, P.M. (Paweł Madejski); validation, M.K., P.M. (Piotr Michalak) and T.K.; formal analysis, P.M. (Paweł Madejski) and P.M. (Piotr Michalak); investigation, P.M. (Paweł Madejski), P.M. (Piotr Michalak) and M.K.; resources, P.M. (Paweł Madejski) and P.M. (Piotr Michalak); data curation, P.M. (Paweł Madejski); writing—original draft preparation, P.M. (Piotr Michalak) and P.M. (Paweł Madejski); writing—review and editing, P.M. (Piotr Michalak) and P.M. (Paweł Madejski); visualization, P.M. (Piotr Michalak) and P.M. (Paweł Madejski); supervision, P.M. (Paweł Madejski); project administration, P.M. (Paweł Madejski); funding acquisition, P.M. (Paweł Madejski) and K.B. All authors have read and agreed to the published version of the manuscript.

Funding: The research leading to these results received funding from the Norway Grants 2014-2021 via the National Centre for Research and Development. The work was prepared within the frame of the project: "Negative CO_2 emission gas power plant"-NOR/POLNORCCS/NEGATIVE-CO2-PP/0009/2019-00, which is co-financed by the programme "Applied research" under the Norwegian Financial Mechanisms 2014–2021 POLNOR CCS 2019-Development of CO2 capture solutions integrated in power and industry processes.

Data Availability Statement: Not applicable.

Conflicts of Interest: The authors declare no conflict of interest.

Nomenclature

$\dot{Q}_C$	heat flux from steam condensation, W
$\dot{Q}_{cond\_c}$	heat flux from water condensate cooling, W
$\dot{Q}_{CO2}$	heat flux from CO_2 condensation, W
$\dot{Q}_s$	heat flux given by the steam, W
$\dot{Q}_{cw}$	heat flux absorbed by the cooling water, W,
$\dot{Q}_{vap\_C}$	heat flux from water vapour cooling, W
T_c	condensate temperature, K
$T_{cw,in}$	temperature of inlet cooling water, K
ΔT	cooling water temperature difference, K
c_w	specific heat of water, J/(kg·K)
d	internal pipe diameter, m,
h_{1CO_2}	carbon dioxide enthalpy at point 1, kJ/kg
h_{3CO_2}	carbon dioxide enthalpy at point 3, J/kg
h_{1H_2O}	water vapour enthalpy at point 1, J/kg
h_{3H_2O}	water vapour enthalpy at point 3, J/kg
h_{sat_liq}	saturated liquid enthalpy, J/kg
h_{sat_vap}	saturated vapour enthalpy, J/kg
K	coverage factor; k = 2 for 95% confidence level of the uncertainty,
$\dot{m}_c$	mass flow rate of the condensate, kg/s

$\dot{m}_{cw}$	mass flow rate of cooling water, kg/s
$\dot{m}_s$	mass flow rate of exhaust steam, kg/s
$\dot{m}_{H_2O}$	water vapour mass flow rate, kg/s
$\dot{m}_{cw}$	cooling water mass flow rate, kg/s
$\dot{m}_{CO_2}$	carbon dioxide mass flow rate, kg/s
u	uncertainty,
U	expanded uncertainty,
r	evaporation energy at saturation pressure, J/kg
$u_{h,table}$	uncertainty of specific enthalpy given in tables, J/kg
$w_{h,table}$	kinematic viscosity, m^2/s
w_r	water velocity, m/s

References

1. Ziembicki, P.; Kozioł, J.; Bernasiński, J.; Nowogoński, I. Innovative System for Heat Recovery and Combustion Gas Cleaning. *Energies* **2019**, *12*, 4255. [CrossRef]
2. Tic, W.J.; Guziałowska-Tic, J. The Cost-Efficiency Analysis of a System for Improving Fine-Coal Combustion Efficiency of Power Plant Boilers. *Energies* **2021**, *14*, 4295. [CrossRef]
3. Damartzis, T.; Asimakopoulou, A.; Koutsonikolas, D.; Skevis, G.; Georgopoulou, C.; Dimopoulos, G.; Nikolopoulos, L.; Bougiouris, K.; Richter, H.; Lubenau, U.; et al. Solvents for Membrane-Based Post-Combustion CO_2 Capture for Potential Application in the Marine Environment. *Appl. Sci.* **2022**, *12*, 6100. [CrossRef]
4. Slavu, N.; Badea, A.; Dinca, C. Technical and Economical Assessment of CO2 Capture-Based Ammonia Aqueous. *Processes* **2022**, *10*, 859. [CrossRef]
5. Czakiert, T.; Krzywanski, J.; Zylka, A.; Nowak, W. Chemical Looping Combustion: A Brief Overview. *Energies* **2022**, *15*, 1563. [CrossRef]
6. Hatta, N.S.M.; Aroua, M.K.; Hussin, F.; Gew, L.T. A Systematic Review of Amino Acid-Based Adsorbents for CO_2 Capture. *Energies* **2022**, *15*, 3753. [CrossRef]
7. Mendiara, T.; García-Labiano, F.; Abad, A.; Gayán, P.; de Diego, L.F.; Izquierdo, M.T.; Adánez, J. Negative CO_2 emissions through the use of biofuels in chemical looping technology: A review. *Appl. Energy* **2018**, *232*, 657–684. [CrossRef]
8. Tramošljika, B.; Blecich, P.; Bonefačić, I.; Glažar, V. Advanced Ultra-Supercritical Coal-Fired Power Plant with Post-Combustion Carbon Capture: Analysis of Electricity Penalty and CO_2 Emission Reduction. *Sustainability* **2021**, *13*, 801. [CrossRef]
9. Madejski, P.; Chmiel, K.; Subramanian, N.; Kuś, T. Methods and Techniques for CO_2 Capture: Review of Potential Solutions and Applications in Modern Energy Technologies. *Energies* **2022**, *15*, 887. [CrossRef]
10. Ziółkowski, P.; Badur, J.; Pawlak-Kruczek, H.; Niedzwiecki, L.; Kowal, M.; Krochmalny, K. A novel concept of negative CO_2 emission power plant for utilization of sewage sludge. In Proceedings of the 6th International Conference on Contemporary Problems of Thermal Engineering CPOTE 2020, Gliwice, Poland, 21–24 September 2020; pp. 531–542.
11. Ziółkowski, P.; Madejski, P.; Amiri, M.; Kuś, T.; Stasiak, K.; Subramanian, N.; Pawlak-Kruczek, H.; Badur, J.; Niedźwiecki, Ł.; Mikielewicz, D. Thermodynamic Analysis of Negative CO2 Emission Power Plant Using Aspen Plus, Aspen Hysys, and Ebsilon Software. *Energies* **2021**, *14*, 6304. [CrossRef]
12. Ziółkowski, P.; Głuch, S.; Ziółkowski, P.J.; Badur, J. Compact High Efficiency and Zero-Emission Gas-Fired Power Plant with Oxy-Combustion and Carbon Capture. *Energies* **2022**, *15*, 2590. [CrossRef]
13. Jacobs, H.R. Direct-Contact Condensation. In *Direct-Contact Heat Transfer*; Kreith, F., Boehm, R.F., Eds.; Springer: Berlin/Heidelberg, Germany, 1988; pp. 223–236. [CrossRef]
14. Desideri, U.; Di Maria, F. Simulation code for design and off design performance prediction of geothermal power plants. *Energy Convers. Manag.* **2000**, *41*, 61–76. [CrossRef]
15. Li, Y.; Klausner, J.F.; Mei, R. Performance characteristics of the diffusion driven desalination process. *Desalination* **2006**, *196*, 188–209. [CrossRef]
16. Ebrahimi, M.; Keshavarz, A.; Jamali, A. Energy and exergy analyses of a micro-steam CCHP cycle for a residential building. *Energy Build.* **2012**, *45*, 202–210. [CrossRef]
17. Marugán-Cruz, C.; Sánchez-Delgado, S.; Gómez-Hernández, J.; Santana, D. Towards zero water consumption in solar tower power plants. *Appl. Therm. Eng.* **2020**, *178*, 115505. [CrossRef]
18. Yan, M.; Ma, C.; Shen, Q.; Song, Z.; Chang, J. A novel lignite pre-drying system integrated with flue gas waste heat recovery at lignite-fired power plants. *Appl. Therm. Eng.* **2019**, *150*, 200–209. [CrossRef]
19. Zhao, X.; Fu, L.; Wang, X.; Sun, T.; Wang, J.; Zhang, S. Flue gas recovery system for natural gas combined heat and power plant with distributed peak-shaving heat pumps. *Appl. Therm. Eng.* **2017**, *111*, 599–607. [CrossRef]
20. Amann, J.M.; Kanniche, M.; Bouallou, C. Natural gas combined cycle power plant modified into an O_2/CO_2 cycle for CO_2 capture. *Energy Convers. Manag.* **2009**, *50*, 510–521. [CrossRef]
21. Garlapalli, R.K.; Spencer, M.W.; Alam, K.; Trembly, J.P. Integration of heat recovery unit in coal fired power plants to reduce energy cost of carbon dioxide capture. *Appl. Energy* **2018**, *229*, 900–909. [CrossRef]

22. Wei, M.; Zhao, X.; Fu, L.; Zhang, S. Performance study and application of new coal-fired boiler flue gas heat recovery system. *Appl. Energy* **2017**, *188*, 121–129. [CrossRef]
23. Prananto, L.A.; Juangsa, F.B.; Iqbal, R.M.; Aziz, M.; Soelaiman, T.A.F. Dry steam cycle application for excess steam utilization: Kamojang geothermal power plant case study. *Renew. Energy* **2018**, *117*, 157–165. [CrossRef]
24. Mati, A.; Buffi, M.; Dell'Orco, S.; Lombardi, G.; Ramiro, P.M.R.; Kersten, S.R.A.; Chiaramonti, D. Fractional Condensation of Fast Pyrolysis Bio-Oil to Improve Biocrude Quality towards Alternative Fuels Production. *Appl. Sci.* **2022**, *12*, 4822. [CrossRef]
25. Thongtip, T.; Aphornratana, S. An experimental analysis of the impact of primary nozzle geometries on the ejector performance used in R141b ejector refrigerator. *Appl. Therm. Eng.* **2017**, *110*, 89–101. [CrossRef]
26. Bencharif, M.; Nesreddine, H.; Perez, S.C.; Poncet, S.; Zid, S. The benefit of droplet injection on the performance of an ejector refrigeration cycle working with R245fa. *Int. J. Refrig.* **2020**, *113*, 276–287. [CrossRef]
27. Klausner, J.F.; Li, Y.; Mei, R. Evaporative heat and mass transfer for the diffusion driven desalination process. *Heat Mass Transf.* **2006**, *42*, 528–536. [CrossRef]
28. Wang, Y.; Hu, Y.; Huang, Q.; Cui, Y. Transient heat transfer study of direct contact condensation of steam in spray cooling water. *Trans. Tianjin Univ.* **2018**, *24*, 131–143. [CrossRef]
29. Hu, Y.; Wang, Y.; Huang, Q.; Cui, Y. Transient analysis of the steam-water direct contact condensation in the packed column. *Can. J. Chem. Eng.* **2018**, *96*, 404–413. [CrossRef]
30. Poškas, R.; Sirvydas, A.; Kulkovas, V.; Jouhara, H.; Poškas, P.; Miliauskas, G.; Puida, E. An Experimental Investigation of Water Vapor Condensation from Biofuel Flue Gas in a Model of Condenser, (2) Local Heat Transfer in a Calorimetric Tube with Water Injection. *Processes* **2021**, *9*, 1310. [CrossRef]
31. Negative CO2 Emission Gas Power Plant. Available online: https://nco2pp.mech.pg.gda.pl/en (accessed on 25 September 2022).
32. Madejski, P.; Kuś, T.; Subramanian, N.; Karch, M.; Michalak, P. The possibilities of carrying out numerical and experimental tests of jet type flow condensers for application in energy technologies. In Proceedings of the Wdzydzeanum Workshop on Fluid-Solid Interaction, Gdańsk, Poland, 5–10 September2021.
33. Madejski, P.; Karch, M.; Michalak, P.; Banasiak, K.; Kuś, T.; Subramanian, N. Measurement techniques and apparatus for experimental studies of flow processes in a system with a jet flow type condenser. In Proceedings of the XIV Multiphase Workshop and Summer School, Koszałkowo–Wieżyca k, Gdańsk, Poland, 2–4 September 2021.
34. Madejski, P.; Kuś, T.; Subramanian, N. Development of the analysis results for the possibility of using spray-ejector condensers for efficient operation in a negative CO_2 emission power plant cycle. In *Report WP1 Task 2*; POLNOR CCS nCO2PP: Kraków, Poland, March 2021.
35. Ziółkowski, P.; Stasiak, K.; Amiri, M.; Dąbrowski, P.; Mikielewicz, D. Completion of the PFD (Process Flow Diagram) along with detailed mass, momentum and energy balance of the negative CO_2 emission gas power plant (nCO2PP) based on steam gasification of sewage sludge, coupled with CCS. In *Report WP1 Task 1*; POLNOR CCS nCO2PP: Gdańsk, Poland, January 2021.
36. National Institute of Standards and Technology, Carbon Dioxide Tables. Available online: https://webbook.nist.gov/cgi/inchi/InChI%3D1S/CO2/c2-1-3 (accessed on 9 September 2022).
37. Helm, I.; Jalukse, L.; Leito, I. Measurement Uncertainty Estimation in Amperometric Sensors: A Tutorial Review. *Sensors* **2010**, *10*, 4430–4455. [CrossRef]
38. Chen, J.; Chen, C. Uncertainty Analysis in Humidity Measurements by the Psychrometer Method. *Sensors* **2017**, *17*, 368. [CrossRef]
39. Chen, L.-H.; Chen, J.; Chen, C. Effect of Environmental Measurement Uncertainty on Prediction of Evapotranspiration. *Atmosphere* **2018**, *9*, 400. [CrossRef]
40. Jing, H.; Quan, Z.; Zhao, Y.; Wang, L.; Ren, R.; Liu, Z. Thermal Performance and Energy Saving Analysis of Indoor Air–Water Heat Exchanger Based on Micro Heat Pipe Array for Data Center. *Energies* **2020**, *13*, 393. [CrossRef]
41. Ali, A.; Cocchi, L.; Picchi, A.; Facchini, B. Experimental Determination of the Heat Transfer Coefficient of Real Cooled Geometry Using Linear Regression Method. *Energies* **2021**, *14*, 180. [CrossRef]
42. Advisory Note No. 1. Uncertainties in Enthalpy for the IAPWS Formulation 1995 for the Thermodynamic Properties of Ordinary Water Substance for General and Scientific Use (IAPWS-95) and the IAPWS Industrial Formulation 1997 for the Thermodynamic Properties of Water and Steam (IAPWS-IF97). The International Association for the Properties of Water and Steam. Vejle, Denmark. August 2003. Available online: http://www.iapws.org/relguide/Advise1.pdf (accessed on 12 September 2022).
43. Wang, J.; Jia, C.-S.; Li, C.-J.; Peng, X.-L.; Zhang, L.-H.; Liu, J.-Y. Thermodynamic Properties for Carbon Dioxide. *ACS Omega* **2019**, *4*, 19193–19198. [CrossRef] [PubMed]
44. Michalski, L.; Eckersdorf, K.; Kucharski, J.; McGhee, J. *Temperature Measurement*, 2nd ed.; John Wiley & Sons Ltd.: Hoboken, NJ, USA, 2001.
45. Lee, T.-W. *Thermal and Flow Measurements*; CRC Press, Taylor & Francis Group, LLC: Boca Raton, FL, USA, 2008.
46. *IEC 60751:2022*; Industrial Platinum Resistance Thermometers and Platinum Temperature Sensors. International Electrotechnical Commission: Geneva, Switzerland, 2022.
47. Nicholas, J.V.; White, D.R. *Traceable Temperatures*; John Wiley & Sons, Ltd.: Chichester, UK, 2001.
48. *IEC 60584-1:2013*; Thermocouples-Part 1: EMF Specifications and Tolerances. International Electrotechnical Commission: Geneva, Switzerland, 2013.
49. Temperature Sensors—Product Catalogue. Limatherm Sensor. Available online: https://www.limathermsensor.pl/files/downloads/Catalogue_temperature_sensors_old.pdf (accessed on 25 September 2022).
50. Sandberg, R.J. *Temperature*; CRC Press LLC: Boca Raton, FL, USA, 2000.

51. Smith, C.L. *Basic Process Measurements*; John Wiley & Sons, Inc.: Hoboken, NJ, USA, 2009.
52. Zosel, J.; Oelßner, W.; Decker, M.; Gerlach, G.; Guth, U. The measurement of dissolved and gaseous carbon dioxide concentration. *Meas. Sci. Technol.* **2011**, *22*, 072001. [CrossRef]
53. Mendes, L.B.; Ogink, N.W.M.; Edouard, N.; Van Dooren, H.J.C.; Tinôco, I.D.F.F.; Mosquera, J. NDIR Gas Sensor for Spatial Monitoring of Carbon Dioxide Concentrations in Naturally Ventilated Livestock Buildings. *Sensors* **2015**, *15*, 11239–11257. [CrossRef]
54. Gerlach, G.; Guth, U.; Oelßner, W. *Carbon Dioxide Sensing: Fundamentals, Principles, and Applications*; Wiley-VCH Verlag GmbH & Co.: Weinheim, Germany, 2019.
55. Pedemonte, A.A.; Traverso, A.; Massardo, A.F. Experimental analysis of pressurised humidification tower for humid air gas turbine cycles. Part A: Experimental campaign. *Appl. Therm. Eng.* **2008**, *28*, 1711–1725. [CrossRef]
56. Pedemonte, A.A.; Traverso, A.; Massardo, A.F. Experimental analysis of pressurised humidification tower for humid air gas turbine cycles. Part B: Correlation of experimental data. *Appl. Therm. Eng.* **2008**, *28*, 1623–1629. [CrossRef]
57. Apanasevich, P.; Coste, P.; Ničeno, B.; Heib, C.; Lucas, D. Comparison of CFD simulations on two-phase Pressurized Thermal Shock scenarios. *Nucl. Eng. Des.* **2014**, *266*, 112–128. [CrossRef]
58. Mahood, H.B.; O Sharif, A.; Alaibi, S.; Hawkins, D.; Thorpe, R.B. Analytical solution and experimental measurements for temperature distribution prediction of three-phase direct-contact condenser. *Energy* **2014**, *67*, 538–547. [CrossRef]
59. Chen, X.; Tian, M.; Zhang, G.; Leng, X.; Qiu, Y.; Zhang, J. Visualization study on direct contact condensation characteristics of sonic steam jet in subcooled water flow in a restricted channel. *Int. J. Heat Mass Transf.* **2019**, *145*, 118761. [CrossRef]
60. Yang, X.P.; Liu, J.P.; Zong, X.; Chong, D.T.; Yan, J.J. Experimental study on the direct contact condensation of the steam jet in subcooled water flow in a rectangular channel: Flow patterns and flow field. *Int. J. Heat Fluid Flow* **2015**, *56*, 172–181. [CrossRef]
61. Xu, Q.; Guo, L.; Zou, S.; Chen, J.; Zhang, X. Experimental study on direct contact condensation of stable steam jet in water flow in a vertical pipe. *Int. J. Heat Mass Transf.* **2013**, *66*, 808–817. [CrossRef]
62. Hu, R.; Jin, Y.; Huang, Q.; Wang, Y.; Cui, Y. The effect of packing on direct contact evaporation in spray column. *Can. J. Chem. Eng.* **2017**, *95*, 2209–2220. [CrossRef]
63. Genić, S. Direct-contact condensation heat transfer on downcommerless trays for steam-water system. *Int. J. Heat Mass Transf.* **2006**, *49*, 1225–1230. [CrossRef]
64. Reddick, C.; Sorin, M.; Sapoundjiev, H.; Aidoun, Z. Effect of a mixture of carbon dioxide and steam on ejector performance: An experimental parametric investigation. *Exp. Therm. Fluid Sci.* **2018**, *92*, 353–365. [CrossRef]
65. Chen, X.; Tian, Z.; Guo, F.; Yu, X.; Huang, Q. Experimental investigation on direct-contact condensation of subatmospheric pressure steam in cocurrent flow packed tower. *Energy Sci. Eng.* **2022**, *10*, 2954–2969. [CrossRef]
66. Datta, P.; Chakravarty, A.; Saha, R.; Chaudhuri, S.; Ghosh, K.; Mukhopadhyay, A.; Sen, S.; Dutta, A.; Goyal, P. Experimental investigation on the effect of initial pressure conditions during steam-water direct contact condensation in a horizontal pipe geometry. *Int. Commun. Heat Mass Transf.* **2021**, *121*, 105082. [CrossRef]
67. Kwidzinski, R. Condensation heat and mass transfer in steam–water injectors. *Int. J. Heat Mass Transf.* **2021**, *164*, 120582. [CrossRef]
68. Zare, S.; Jamalkhoo, M.H.; Passandideh-Fard, M. Experimental Study of Direct Contact Condensation of Steam Jet in Water Flow in a Vertical Pipe With Square Cross Section. *Int. J. Multiph. Flow* **2018**, *104*, 74–88. [CrossRef]
69. Zong, X.; Liu, J.-P.; Yang, X.-P.; Yan, J.-J. Experimental study on the direct contact condensation of steam jet in subcooled water flow in a rectangular mix chamber. *Int. J. Heat Mass Transf.* **2015**, *80*, 448–457. [CrossRef]